In-situ desalination-coupled electrolysis with concurrent one-step-synthesis of value-added chemicals

Byeong-ju Kim [a], Ho Kyong Shon [b], Dong Suk Han [c,*], Hyunwoong Park [a,*]

[a] *School of Energy Engineering, Kyungpook National University, Daegu 41566, Republic of Korea*
[b] *School of Civil and Environmental Engineering, University of Technology, Sydney, Post Box 129, Broadway, Sydney, NSW 2007, Australia*
[c] *Center for Advanced Materials and Department of Chemical Engineering, Qatar University, P.O. Box 2713, Doha, Qatar*

HIGHLIGHTS

- A multi-functional electrolyzer (NiFe-LDH/BPM/[AEM/CEM]$_n$/BPM/NiMo) is designed.
- A NiFe-LDH-NiMo pair drives OER and HER, respectively, at a Faradaic efficiency of >95 %.
- The initial pH values of anolyte and catholyte remain unchanged.
- Desalination of saline water proceeds with a specific energy consumption of 1.8 kWh m^{-3}.
- HCl and NaOH are concurrently produced.

GRAPHICAL ABSTRACT
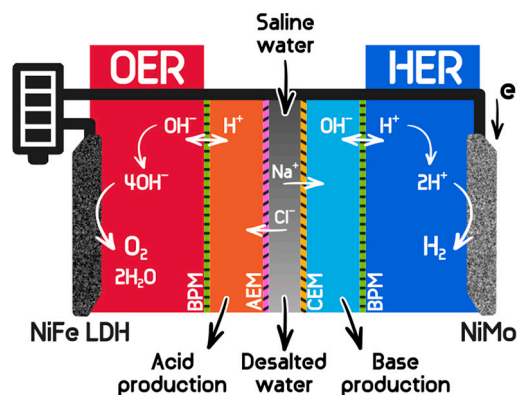
ARTICLE INFO

ABSTRACT

An efficient multi-functional electrolyzer with a Ni- and Fe-layered double hydroxide (NiFe-LDH) anode and a binary NiMo cathode is designed for overall water splitting coupled with the desalination of saline water and production of value-added chemicals. The NiFe-LDH and NiMo pairs separated by a bipolar membrane (BPM) show overpotentials as low as those of noble metal catalysts for oxygen and hydrogen evolution reactions in 1 M KOH and 1 M H$_2$SO$_4$ solutions, respectively. Arraying anion and cation-exchange membranes (AEMs and CEMs, respectively) with BPMs (NiFe-LDH/BPM/[AEM/CEM]$_n$/BPM/NiMo; $n = 1$ or 5) further enables the desalination of brackish water and seawater at specific energy consumption of 1.8 kWh m^{-3}, with concurrent production of HCl and NaOH. The Faradaic efficiencies of the device for O$_2$ and H$_2$ production are >95 % at $J = 100$ mA cm^{-2} over 20 h, while the initial pH values of the anolyte and catholyte remain unchanged. Detailed surface characterization of the electrocatalysts is performed, and various electrolyzer configurations are compared in terms of desalination efficiency.

1. Introduction

The global demand for molecular hydrogen has increased >3-fold since the mid-1970s and natural gas is still the largest hydrogen source (~75 %), followed by coal and oil [1,2]. This fossil-fuel oriented, carbon-footprinted hydrogen does not contribute to the mitigation of CO_2 emissions, and its production cost varies significantly depending on geopolitical status. Water electrolysis has long been considered the most viable alternative to gray hydrogen production processes [3–5]. Most natural water and wastewater contain chloride as a main constituent, for example, at concentrations of approximately 1 mM in rivers and lakes, 5 mM in agricultural water, 0.03 M in human urine, 0.45 M in textile wastewater, 0.5 M in seawater [6]. The electrolysis of these salt water is challenging [7–10], particularly because of the chloride oxidation reaction (ClOR; $Cl^- + H_2O \rightarrow HClO + H^+ + 2e^-$, $E° = 1.482$ V) competitive with the oxygen evolution reaction (OER; $2H_2O \rightarrow O_2 + 4H^+ + 4e^-$, $E° = 1.229$ V) [6,11–14]. Besides, scale layers ($CaCO_3$ and $Mg(OH)_2$) are readily formed on the cathode, where the local pH is higher than the bulk pH due to the interfacial hydrogen evolution reaction (HER) [15,16].

To address these challenges, desalination-coupled electrolysis has been proposed and proven to be technically viable. A recent study estimated that the direct capital and operation costs of the reverse osmosis are trivial, leading to an insignificant contribution to the levelized H_2 cost (<0.1 \$ per kg H_2) [17]. Hausmann et al. further analyzed that the two-step process of reverse osmosis desalination and electrolysis was technically more feasible than the direct saline water electrolysis [18]. Forward osmosis-coupled in-situ electrolysis also has been demonstrated as a viable approach without pretreatment and with minimal losses in energy efficiency [19].

We propose a different type of electrolysis coupled with anion- and cation-exchange membranes (AEMs and CEMs, respectively) and bipolar membranes (BPMs) (Scheme 1). An electrochemical bias to the anode and cathode pairs causes unidirectional transport of Cl^- and Na^+ from the desalination cell to the acid and base cells across the AEM and CEM, respectively [12,20,21]. The bias further dissociates water ($H_2O \rightarrow H^+ + OH^-$) sorbed in the BPMs, supplying the anolyte with OH^-, acid cell with H^+, base cell with OH^-, and catholyte with H^+ [22–24]. Although the proposed membrane-coupled electrolysis does not use saline water as a feedstock, it has four unique advantages. First, the OER can proceed while the competitive ClOR is effectively inhibited, even without artificial alkalization of saline water. Second, the anolyte and catholyte maintain alkaline (pH ~14) and acidic (pH ~0.5) conditions owing to the continual supply of OH^- and H^+, respectively, from the BPMs. This function of the BPMs is well known. Such a pH difference of ~13.5 should be beneficial, particularly in reducing the OER overpotential (η_{OER}). Third, in addition to H_2 production in the catholyte cell, HCl and NaOH are obtained from the acid and base cells, respectively. Although the concurrent production of acid and base can be achieved by appropriately aligning BPMs and ion-exchange membranes, these value-added chemicals should improve the cost-effectiveness of the electrolysis system. Finally, various types of saline water, including brackish water, seawater, and brine, can be used, and the as-obtained value-added desalted water can further contribute to reducing freshwater scarcity
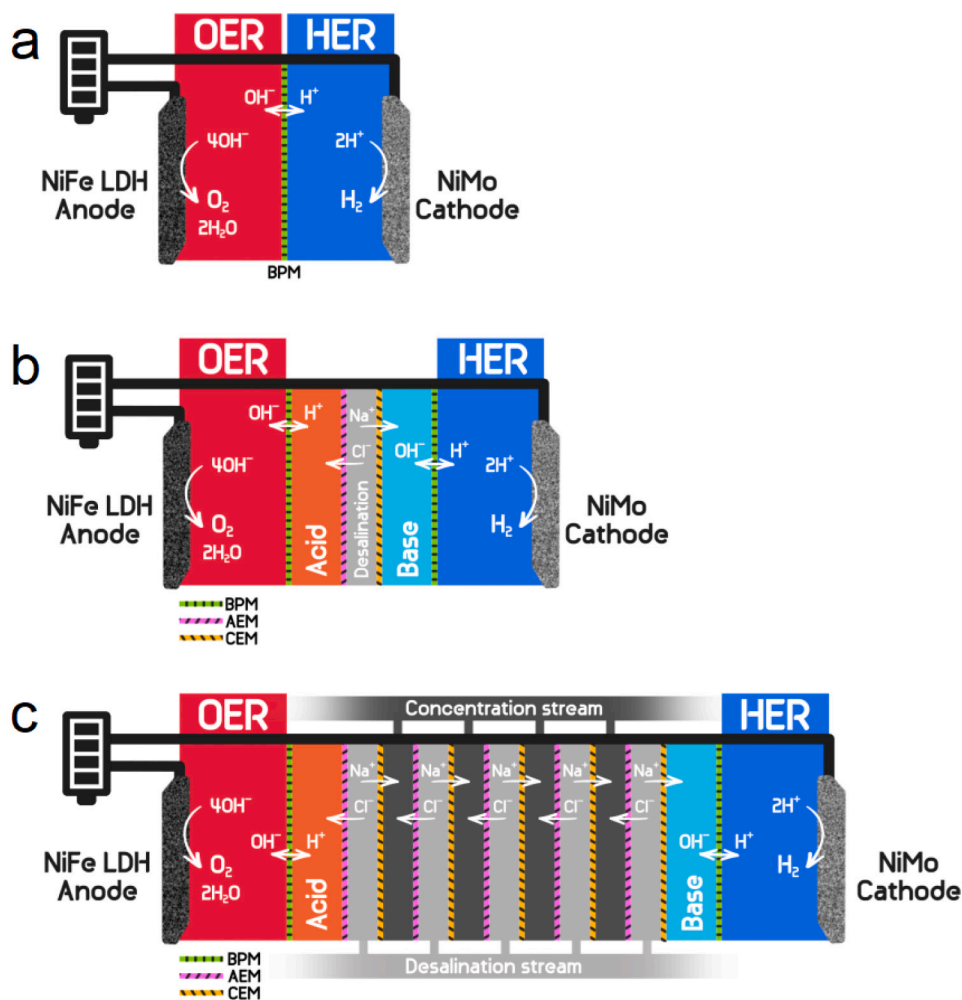
Scheme 1. Schematic illustration of the as-designed electrolyzers comprising NiFe-LDH anode in an alkaline solution (1 M KOH) and NiMo cathode in an acidic solution (1 M H_2SO_4). (a) Two-cell electrolyzer divided by a BPM. (b) Desalination-coupled electrocatalytic unit device with (from left) a BPM, AEM, CEM, and BPM. (c) Desalination-coupled electrocatalytic stack device. The five desalination cells are stacked by alternately inserting AEMs and CEMs between acid and base cells. Sandwiched cells between adjacent two desalination cells are denoted as concentration cells. In b and c, all solutions (except for anolyte and catholyte) are circulated.

[25,26].

For electrolysis, we synthesized Ni- and Fe-layered double hydroxides (NiFe-LDH) and binary NiMo metals as OER and HER electrocatalysts, respectively, via electrodeposition onto Ni foam substrates. 3d-transition metal (Ni, Co, Fe, and Mn)-based (oxy)hydroxides usually exhibit low η_{OER} in alkaline media, and their activities are comparable to those of noble metals (e.g., IrO_2 and RuO_2) [27–29]. Particularly, NiFe-LDH is characterized by abundant active sites for OH adsorption and an optimal binding energy for M-OH [29,30]. Meanwhile, loading bimetallic NiMo on an active electrode for the HER has been known to improve the electrocatalytic activity and durability owing to its high surface area [21,31–33]. The loaded Ni and Mo can induce electronic synergy, leading to suitable hydrogen adsorption energy and hydrogen spill-over effect [33]. The as-synthesized NiFe-LDH anode and NiMo cathodes were equipped into the as-designed membrane cell arrays with saline water. All individual reactions (desalination, OER, and HER) occurred successfully, with low overall specific energy consumption for desalination, while concurrently producing HCl and NaOH.

2. Experimental

2.1. Synthesis of electrocatalysts

Ni foams (1×1 cm^2, >99.99 %, 1.6 mm thick, MTI Korea Co., Ltd.) connected with a nickel wire (99.5 %, 0.5 mm diameter, Alfa Aesar) were ultrasonically treated with HCl (1 M, Daejung) for 10 min, rinsed with deionized water (18 MΩ cm, Human Corp.) and ethanol, and dried for 10 min at ~60 °C. To electrodeposit NiFe-LDHs, the as-prepared Ni substrates (for the working electrode) were immersed in aqueous mixed solutions (100 mM) with nickel(II) chloride hexahydrate ($NiCl_2 \cdot 6H_2O$, 23–26 % Ni basis, Sigma-Aldrich) and/or iron(III) nitrate nonahydrate ($Fe(NO_3)_3 \cdot 9H_2O$, ≥98 %, Sigma-Aldrich) at various molar ratios of Ni/Fe (1/0, 0.75/0.25, 0.5/0.5, 0.25/0.75, and 0/1). They were then cathodically biased with $J = -100$ mA cm^{-2} for 10–180 s. A saturated calomel electrode (SCE) and a Pt foil were used as the reference and counter electrodes, respectively. The as-deposited NiFe-LDHs were anodized at $J = 10$ mA cm^{-2} for 5 min in an aqueous KOH solution (1 M, pH ~13.7, Daejung). Unless otherwise specified, NiFe-LDH in this study refers to the sample synthesized at a Ni/Fe ratio of 0.5/0.5 deposited for 120 s. For the electrosynthesis of NiMo, the Ni substrates were immersed in aqueous mixed solutions containing $NiCl_2 \cdot 6H_2O$ (120 mM, 23–26 % Ni basis, Sigma-Aldrich), sodium molybdate dihydrate (80 mM, $Na_2MoO_4 \cdot 2H_2O$, ≥99.5 %, Sigma-Aldrich), and sodium citrate tribasic dihydrate (120 mM, HOC(COONa)(CH$_2$COONa)$_2 \cdot 2H_2O$, ≥99.0 %, Sigma-Aldrich), and biased with $J = -120$ mA cm^{-2} for 20 min. The solution pH was adjusted to 10.5 using ammonium hydroxide (NH_4OH, ≥25 % NH_3 in H_2O, Sigma-Aldrich) [34]. Finally, the as-synthesized NiFe-LDH and NiMo were rinsed with deionized water and air-dried.

2.2. Surface characterization

The morphology and elemental composition of the as-synthesized samples were examined using field-emission scanning electron microscopy (FE-SEM, S-4800, Hitachi) at an accelerating voltage of 5 kV with an energy dispersive spectrometer (EDS). Field-emission transmission electron microscopy (FE-TEM, 200 kV, Titan G2 with ChemiSTEM Cs Probe, FEI Company) equipped with high-angle annular dark-field scanning transmission electron microscopy (HAADF-STEM), selected area electron diffraction (SAED), and high-resolution transmission electron microscopy (HR-TEM) was used to characterize the morphology and crystalline structure of the as-synthesized samples. To further examine their elemental binding states and crystalline structures, the samples were characterized by X-ray photoelectron spectroscopy (XPS, NEXSA, ThermoFisher) and X-ray diffraction (XRD, EMPYREAN, PANalytical), respectively. The surface area and average pore size of the samples were evaluated using the Brunauer–Emmett–Teller (BET) and Barrett–Joyner–Halenda (BJH) analyzers, respectively, with N_2 adsorption–desorption (Quantachrome).

2.3. Electrochemical reaction and analysis

Linear sweep voltammograms (LSVs) of the as-synthesized NiFe-LDH and NiMo electrodes (working electrodes) were obtained in aqueous 1 M KOH (Daejung) and 1 M H_2SO_4 (Daejung) solutions, respectively, with SCE (reference electrode) and Pt foil (counter electrode), using a potentiostat (Ivium). Potentials were swept from 0.6 V to 0.1 V vs. SCE for NiFe-LDH and from −0.1 V to −0.7 V vs. SCE for NiMo, at a scan rate of 1 mV s^{-1}. Tafel plots were obtained from the LSV data. The electrochemical double-layer capacitance (C_{dl}) values were estimated from the cyclic voltammograms (CVs) of each sample at various scan rates (5–30 mV s^{-1}) in the non-Faradaic region of a 0.1 V-window. Bulk electrolysis for the OER with 1 M KOH or the HER with 1 M H_2SO_4 at $J = 10$ mA cm^{-2} was carried out in a customized, single-cell Teflon reactor. Prior to the initiation of electrolysis, the electrolyte was purged with N_2 gas (>99.99 %) for 30 min. During the electrochemical reactions, the gases evolved from the electrolytes were periodically sampled and quantified using gas chromatography (GC, Agilent 7820A). The electrocatalytic activities and stabilities of the NiFe-LDH and NiMo cathode pairs were tested at $J = 10$ and 100 mA cm^{-2} in a two-cell Teflon reactor separated by a BPM (Fumasep FBM, FuMA-Tech) to maintain the initial pH values of the anolyte (1 M KOH) and catholyte (1 M H_2SO_4) (Scheme 1a).

A desalination-coupled electrochemical unit device was designed. It comprises an anode cell with NiFe-LDH/BPM/acid cell/AEM (AMI-7001S, Membrane International)/desalination cell/CEM (CMI-7000S, Membrane International)/base cell/BPM/cathode cell with NiMo (Scheme 1b). When necessary, the five desalination cells were stacked by alternately inserting AEMs and CEMs between the acid and base cells (NiFe-LDH/BPM/[AEM/CEM]$_n$/BPM/NiMo; $n = 5$) (Scheme 1c). The cells located between adjacent desalination cells were denoted as concentration cells. The anolyte and catholyte of 1 M KOH (20 mL) and 1 M H_2SO_4 (20 mL), respectively, were batch type (uncirculated). In contrast, the solutions in the acid cell (20 mL) and base cell (20 mL) (Table 1) were circulated at a flow rate of 10 mL min^{-1} using a peristaltic pump (Reglo ICC, ISMATEC®). Two saline water streams in the desalination cells (40 mL, 0.171 M NaCl or 10 g L^{-1}, considered as the typical concentration of brackish water) and concentration cells (40 mL, 0.171 M NaCl) were also circulated at a flow rate of 10 mL min^{-1} [35]. To examine the effect of the solution conductivity in the acid and base cells on the desalination performance, 0.1 and 0.2 M NaCl (lower and higher, respectively, than 0.171 M NaCl in the desalination cell) were used (Case Study I vs. II). Instead of 0.1 M NaCl in both the acid and base cells, 0.1 M HCl in the acid cell and 0.1 M NaOH in the base cell were tested to examine the effect of initial pH value (Case Study I vs. III). When necessary, artificial seawater (Instant Ocean Sea Salt, salinity of 36 g L^{-1}) was used as a saline water. The stacks with the NiFe-LDH anode and NiMo cathode were operated at $J = 10$ mA cm^{-2} or 100 mA cm^{-2} using the potentiostat. The ionic conductivity of saline water in the desalination cell and the pH values of the solutions in the acid and base cells were recorded using a pH-conductivity meter (SevenCompact™ S213, METTLER TOLEDO™). When necessary, the solutions in the acid and base cells were periodically sampled and analyzed using ion chromatography (IC; Thermo Scientific, DIONEX ICS-1100) to identify and quantify the transported ions. The overall process was terminated when the ionic conductivity of the saline water reached ~500 μS cm^{-1}.

The Faradaic efficiency (FE) of the evolved O_2 and H_2 gases, specific energy consumption (SEC), and ion transport efficiency (ITE) were calculated using the following equations:

$$FE\ (\%) = (\text{amount of evolved gas} \times 2 \times F) \times (J \times A \times t)^{-1} \times 100\% \quad (1)$$

Table 1
Performance comparison of desalination-coupled electrocatalytic stack devices.

Case study	Saline water	Saline water volume (mL)	Acid cell	Base cell	Desalination cell number	J (mA cm^{-2})	$\tau_{1/2}$ (h)[a]	ITE (%)[a]	SEC (kWh m^{-3})[a]
I	0.171 M NaCl	20	0.1 M NaCl	0.1 M NaCl	1	10	5.4	85	6.58
II	0.171 M NaCl	20	0.2 M NaCl	0.2 M NaCl	1	10	5.6	82	7.03
III	0.171 M NaCl	20	0.1 M HCl	0.1 M NaOH	1	10	5.4	85	6.62
IV	0.171 M NaCl	20	0.1 M HCl	0.1 M NaOH	1	100	0.6	77	15.79
V	0.171 M NaCl	40	0.1 M NaCl	0.1 M NaCl	5	10	2.2	417	1.79
VI	Seawater	40	0.1 M NaCl	0.1 M NaCl	5	10	6.4	358	5.31

[a] For 50 % desalination of saline water.

$$\text{SEC} \ (\text{kWh m}^{-3}) = E_{device} \times J \times \text{A} \times \tau_{1/2} \times (\text{saline water volume})^{-1} \quad (2)$$

$$\text{ITE} \ (\%) = (\text{number of transported charges}) \times (J \times \text{A} \times t)^{-1} \times 100\% \quad (3)$$

where F, E_{device}, J, A, and $\tau_{1/2}$ are the Faraday constant (96,485 C mol^{-1}), device voltage (V), current density (mA cm^{-2}), area (cm^2), and operation time for 50 % desalination (s), respectively. The electrochemical potential versus SCE was converted to that versus reversible hydrogen electrode (RHE) using the following equation: V vs. RHE = V vs. SCE + 0.241 + 0.0591 × pH. Unless otherwise specified, "vs. RHE" is omitted for simplicity.

3. Results and discussion

3.1. Surface and electrochemical characterization of the as-synthesized catalysts

The as-deposited and post-anodized binary NiFe samples were examined by XRD (Fig. 1a). Both samples exhibited identical diffraction patterns, which corresponded to the NiFe-LDH structure (2θ = 34.4° (012), 39.0° (015), and 61.3° (113); ICDD no. 00-040-0215). XPS analysis revealed that Ni^0 (852.9 eV) and Ni^{2+} (856.4, 874.1 eV; respectively for 2p3/2 and 2p1/2) states were mixed in the as-deposited sample (Fig. 1b) [36,37]. The Ni^0 state is attributed to the reduction of Ni^{2+} during the cathodic deposition process. However, the Ni^0 state was not observed and the Ni^{2+} state became dominant in the post-anodized sample. In contrast, only Fe^{3+} states were observed in both samples. The O 1s spectra further showed the co-presence of oxygen atoms associated with metal (M-O with 28.7 %), adsorbed hydroxyl (M-OH with 38.4 %), and H$_2$O (32.8 %) with the as-deposited sample (Fig. 1c). The same oxygen pattern was found for the post-anodized sample, except for a relatively large fraction of M-O (58.7 %) due to partial shifts of Ni^0 and Ni(OH)$_2$ to NiOOH, and Fe(OH)$_3$ to FeOOH [38–41]. The post-anodization process shifted the binding energies of Ni, Fe, and O in the low-energy direction, indicating structural rearrangement of the deposited NiFe-LDH. Notably, the C$_{dl}$ value with the post-anodized NiFe-LDH was estimated to be >20-fold greater than that with the as-deposited one (0.79 vs. 0.037 mF cm^{-2}) (Fig. 1d). Considering the proportional relationship between C$_{dl}$ and the electrochemically active surface area, anodization should be effective in enhancing the electrode/solution interfacial area. Post-anodization slightly reduced the BET area but increased the pore diameter (Figs. S1–S3).

The FE-SEM images of the post-anodized NiFe-LDH showed that the porous Ni substrate was covered with aggregates composed of ~50 nm-sized fine particles (Fig. 2a and b). The HR-TEM and HAADF-STEM
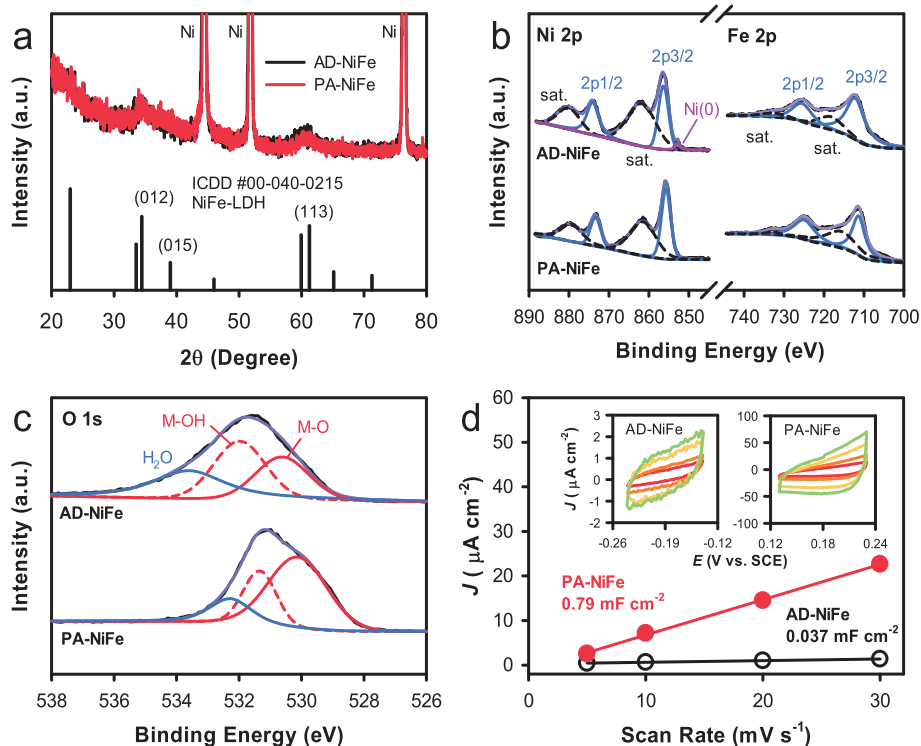

Fig. 1. Surface characterization of the as-deposited (AD) and post-anodized (PA) NiFe-LDH samples. (a) XRD spectra. (b and c) XPS spectra of Ni 2p and Fe 2p (b), and O 1s (c). (d) Effect of scan rates (5–30 mV s^{-1}) on capacitive J in non-Faradaic regions. Numbers on graphs indicate C$_{dl}$ values. Inset shows cyclic voltammograms with different scan rates.
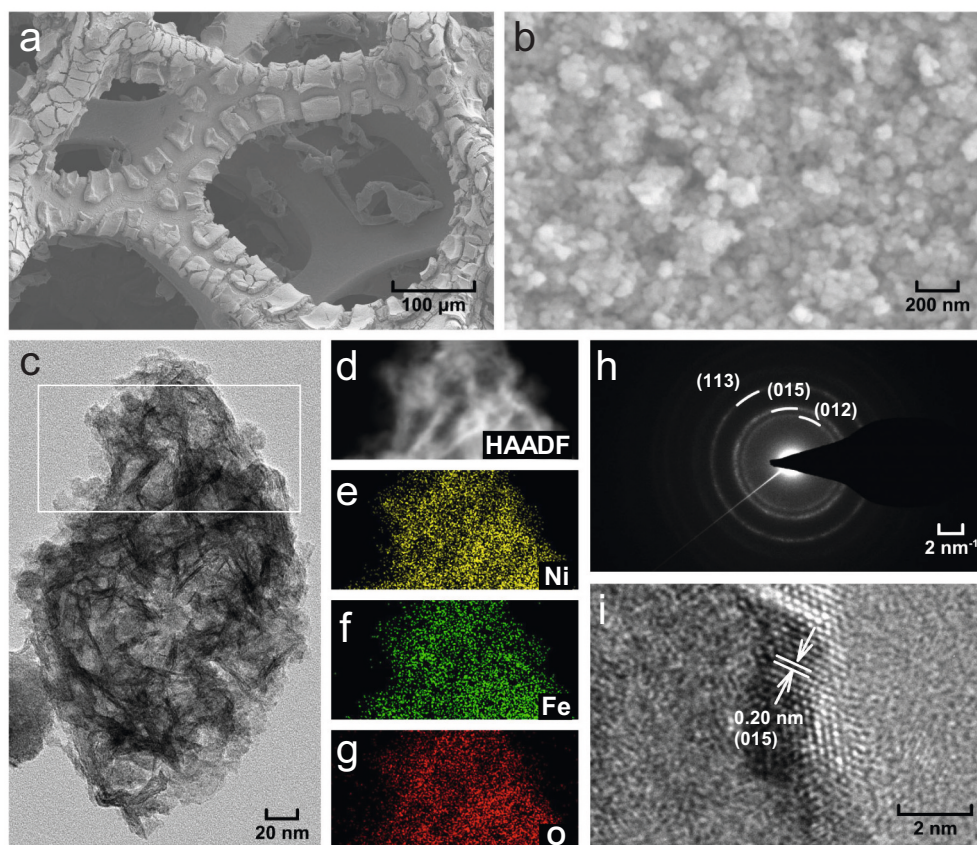
Fig. 2. Surface characterization of post-anodized NiFe-LDH samples. (a and b) FE-SEM images. (c) TEM image. (d-g) HAADF-STEM image and corresponding EDS elemental mappings for the white rectangular region in (c). (h) SAED pattern. (i) HR-TEM image.

images of the NiFe particles collected from the Ni substrate exhibited layered nanostructures (Fig. 2c and d). EDS elemental mapping of the HAADF-STEM image further showed evenly distributed Ni, Fe, and O (Fig. 2e–2g). The Fe fraction in the sample synthesized at an Fe fraction of 0.5 (i.e., Fe/(Ni + Fe)) was estimated to be ~0.3 (Table S1). This value was similar to that estimated by XPS (~0.33) yet significantly lower than that estimated by the FE-SEM (~0.65). Such differences can be attributed to the different analytical principles and techniques. The SAED pattern of the NiFe-LDH sample also showed the presence of (012), (015), and (113) planes associated with amorphous NiFe-LDH (Fig. 2h). The (015) plane was further confirmed by an HR-TEM image with a lattice spacing distance of 0.20 nm (Fig. 2i).

The NiFe-LDH electrodes exhibited different voltammograms depending on the Ni/Fe ratio and deposition time (Fig. 3a–c). For the voltammograms, the electrodes were held at 1.64 V for 20 s and then cathodically swept to separate OER from the Ni redox reactions and accurately estimate η_{OER}. At a Ni/Fe ratio of 1/0 (i.e., Ni only), a cathodic peak was observed at ~1.25 V. This peak slightly shifted to a low potential with increasing deposition time (Fig. 3a). The same peaks were also observed with a Ni/Fe ratio of 1/1; however, the peak intensity and degree of peak shift were less significant (Fig. 3b). With only Fe, this behavior completely vanished (Fig. 3c) (see Fig. S4 for all Ni/Fe ratios). Hence, the cathodic peaks should result solely from the reduction of the oxidized Ni species (e.g., $Ni^{3+} \rightarrow Ni^{2+}$). The η_{OER} at $J = 10$ mA cm^{-2} and 100 mA cm^{-2} (η_{10} and η_{100}, respectively) varied significantly depending on the synthesis conditions. The lowest η_{10} and η_{100} values (~200 mV and ~280 mV, respectively) were obtained with a Ni/Fe ratio of 1/1 at deposition times of >120 s (Fig. S5). These values were significantly lower than those obtained with the Ni substrate and Pt, and were comparable to those reported in the literature [32]. The Tafel plots further show the lowest slope with the NiFe-LDH with a Ni/Fe ratio of 1/

1 (39.9 mV dec^{-1}) among the tested electrodes (Fig. 3d). The lowest slope indicates that electrocatalytic charge transfer occurs most efficiently on the (oxy)hydroxide surface of NiFe-LDH [42]. Bulk electrolysis with the optimized NiFe-LDH was also carried out to examine the OER in a 1 M KOH solution (Fig. 3e). At $J = 10$ mA cm^{-2}, an E of 1.51 V was maintained, while O_2 was continuously produced with a FE of >80 %.

NiMo cathodes have also been synthesized via electrodeposition on porous Ni substrates. The as-synthesized NiMo samples exhibited a granular surface with a particle size of ~2 μm (Fig. 4a). The XRD spectra displayed a typical pattern of intermetallic alloy NiMo (Ni$_{0.88}$Mo$_{0.12}$; 2θ = 43.7° (111), 51.0° (200), and 75.0° (220); ICDD no. 04–023-7853), with overlapping peaks originating from the Ni substrate (Fig. 4b). SEM-EDS elemental analysis estimated a Mo fraction of ~0.1 (Table S1), which was consistent with the XRD pattern. According to the XPS analysis, the Ni 2p spectrum was composed of Ni^0 and Ni^{2+} (Fig. 4c). The Mo 3d spectrum was also composed of Mo^0 and Mo^{6+} (Fig. 4d). Although cathodically deposited, NiMo was partially oxidized in the atmosphere before XPS analysis. The Ni/Mo ratio in the XPS spectra was 0.82/0.18 (Table S1), consistent with the ratios based on the SEM-EDS analysis and the crystalline structure with the XRD.

The electrocatalytic activity of the as-synthesized NiMo electrode was examined and compared with that of a porous Ni substrate and Pt in a 1 M H$_2$SO$_4$ solution. The onset potentials (E_{ons}) of the Ni substrate and NiMo were estimated to be −0.006 V and 0.060 V, respectively (Fig. 5a). Notably, η_{10} and η_{100} with the Ni substrate were as large as −198 mV and −331 mV, respectively, whereas those with NiMo were only −59 mV and −200 mV, respectively. The Tafel slopes for the Ni substrate and NiMo electrodes were estimated to be ~123 mV dec^{-1} and 85 mV dec^{-1}, respectively (Fig. 5b), confirming faster electrocatalytic reaction kinetics with NiMo. For comparison, the Pt electrode exhibited η_{10} and
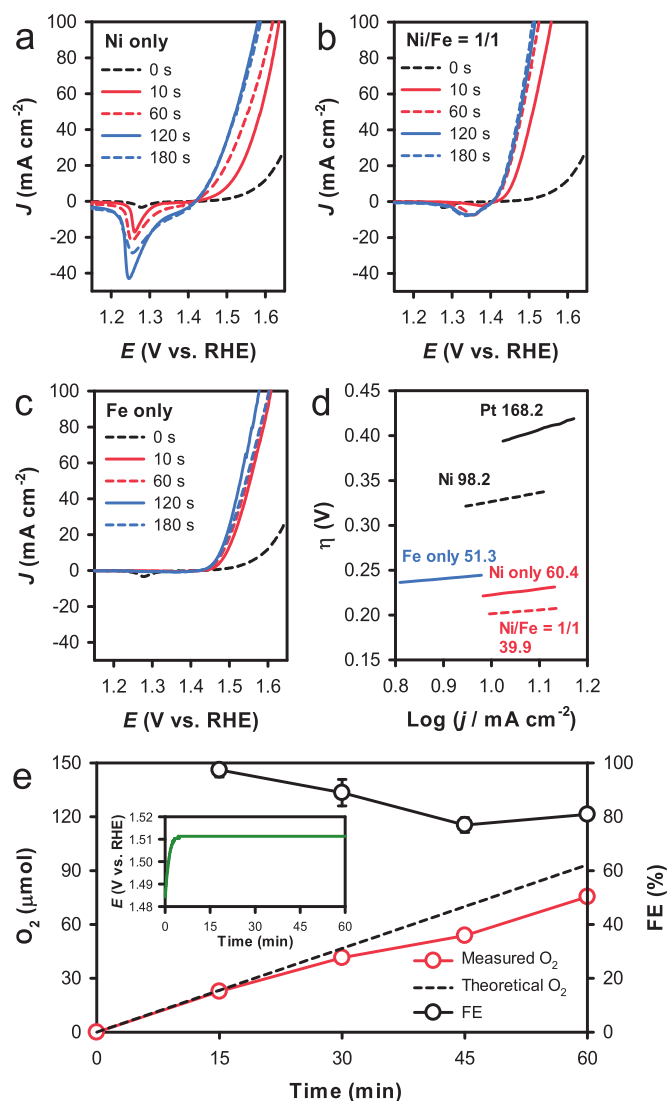
Fig. 3. (a–c) Effects of deposition times on linear sweep voltammograms with NiFe-LDH electrodes deposited with (a) Ni only, (b) Ni and Fe, and (c) Fe only. (d) Tafel plots with NiFe-LDH electrodes (Ni only, Fe only, and Ni/Fe of 1/1). For comparison, Tafel plots with Ni substrate and Pt electrode were also examined. Numbers are Tafel slopes (mV dec^{-1}). (e) O_2 evolution with a NiFe-LDH electrode (Ni/Fe ratio of 1/1) and Faradaic efficiencies (FEs) for OER at J = 10 mA cm^{-2}. Inset shows time-profiled E changes. Electrolyte: 1 M KOH.

Fig. 4. Surface characterization of the as-synthesized NiMo catalysts. (a) FE-SEM images, (b) XRD, and (c and d) XPS spectra of Ni 2p and Mo 3d.

η_{100} of −24 mV and −116 mV, respectively, with an E_{on} of 0.05 V. The H_2 production with NiMo was also examined at J = −10 mA cm^{-2}. The H_2 gas was evolved linearly with time and the FE of the HER was 80–90 %, while an E_{10} between −0.04 V and −0.05 V was maintained (Fig. 5c).

3.2. Coupling NiFe-LDH and NiMo via BPM

The NiFe-LDH anode and NiMo cathode were placed in 1 M KOH and 1 M H_2SO_4, respectively, and both electrolytes were separated using a BPM (Scheme 1a). The J-E_{device} curve with the pair showed the E_{on} of ~1.3 V, while E_{device} values of ~1.5 V and 2.1 V were observed for J = 10 mA cm^{-2} and 100 mA cm^{-2}, respectively (Fig. 6a). A prolonged bulk electrolysis with the NiFe-LDH and NiMo pair at J = 100 mA cm^{-2} produced O_2 and H_2 in the anolyte and catholyte, respectively, at the stoichiometric ratio with FE values of >95 % over 20 h (Fig. 6b). During the electrolysis, the stable E_{device} of ~2.12 V was maintained (Fig. 6c). Note that the NiFe-LDH electrode was pre-anodized in 1 M KOH solution before the electrolysis and successfully reused for 20 h-electrolysis.
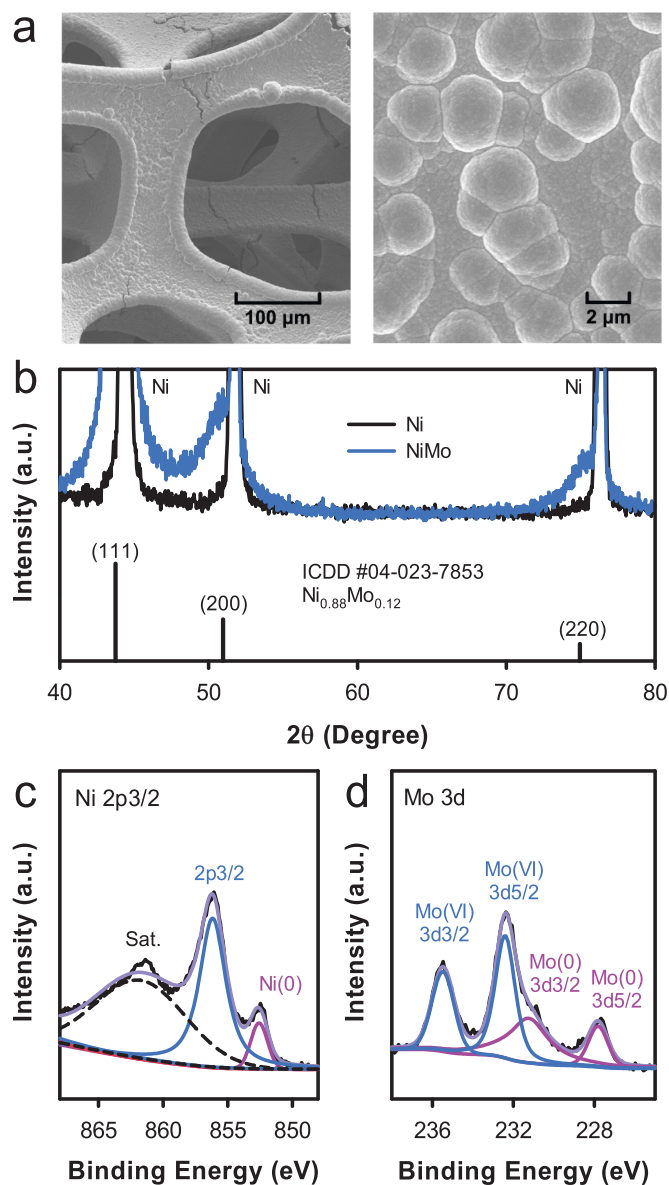
Meanwhile, the NiMo electrode exhibited a negligible change in potential (Δ10 mV) during HER (Fig. 5c inset). These stabilities of the NiFe-LDH and NiMo electrodes should result in the constant E_{device} value. Despite H^+ generation via the OER in the anolyte and H^+ consumption in the catholyte via the HER, the initial pH values of each electrolyte were maintained over 20 h. A pair of Pt anode and Pt cathode was also examined (Fig. 6a). The Pt-Pt pair showed larger E_{on} (>1.6 V) and E_{device} values (~1.7 V and ~2.43 V at J = 10 mA cm^{-2} and 100 mA cm^{-2}, respectively) than the NiFe-LDH and NiMo pairs. Considering that the electrochemical activity of NiMo was slightly lower than that of Pt (Fig. 5a), the superior performance of the NiFe-LDH and NiMo pair to the Pt-Pt pair can be attributed to the far higher activity of the NiFe-LDH anode than that of the Pt anode. The Ni-Ni pair was also tested, and its activity was found to be low. Despite these behaviors of the Pt-Pt pair and Ni-Ni pair, the pH values of the anolyte and catholyte remained unchanged over 20 h when both electrolytes were separated by a BPM (Fig. S6).

Instead of the BPM, other types of ion-exchange membranes (AEM, CEM, and PEM) were examined for bulk electrolysis with NiFe-LDH and
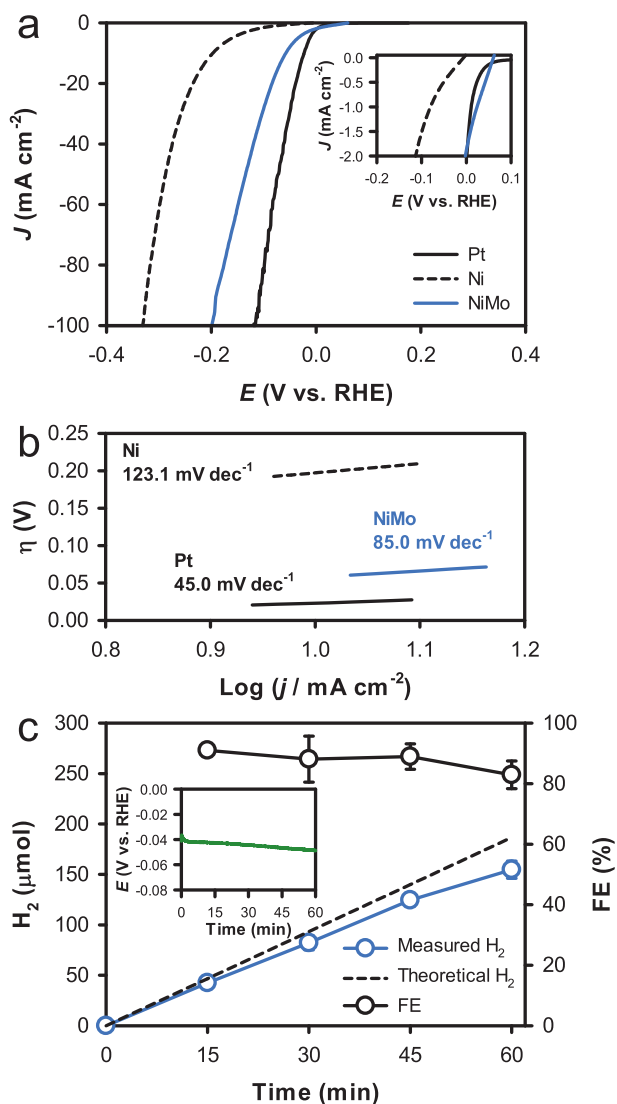
Fig. 5. (a) Linear sweep voltammograms of NiMo, Ni, and Pt electrodes. Inset shows magnified voltammograms near E_{on} regions. (b) Tafel plots with NiMo, Ni, and Pt electrodes. (c) H$_2$ evolution with NiMo electrode and FEs for HER at $J = -10$ mA cm^{-2}. Inset shows time-profiled changes in E. Electrolyte: 1 M H$_2$SO$_4$.

NiMo pairs at $J = 100$ mA cm^{-2} (Fig. S7). For all three membranes, E_{device} gradually increased and then abruptly jumped to >3 V. The anolyte (1 M KOH) pH gradually decreased and suddenly dropped to <3, whereas the catholyte (1 M H$_2$SO$_4$) pH remained relatively unchanged, likely because of the high proton concentration. The same temporal changes in E_{device} and anolyte pH suggest that decreases in anolyte pH caused the dissolution and deactivation of the NiFe-LDH anode, and consequently, the dramatic increase in E_{device}. The anolyte pH changes were attributed to the consumption of hydroxides by the OER (4OH$^-$ → O$_2$ + 2H$_2$O + 4e$^-$). To maintain charge neutrality during electrolysis, different types of ions were transported between the anolyte and catholyte across the membranes. For the AEM, ~0.3 M SO$_4^{2-}$ was found in the anolyte after 4 h (Fig. 6d), whereas K$^+$ was not found in the catholyte. For CEM and PEM, 0.7–0.8 M K$^+$ was transported to the catholyte, whereas SO$_4^{2-}$ transport was effectively retarded. In contrast, the transport of both K$^+$ and SO$_4^{2-}$ across the BPM was significantly inhibited. This should be attributed to the continual supply of OH$^-$ and H$^+$ during electrolysis, maintaining charge neutrality, and consequently, the stability of the NiFe-LDH anode.
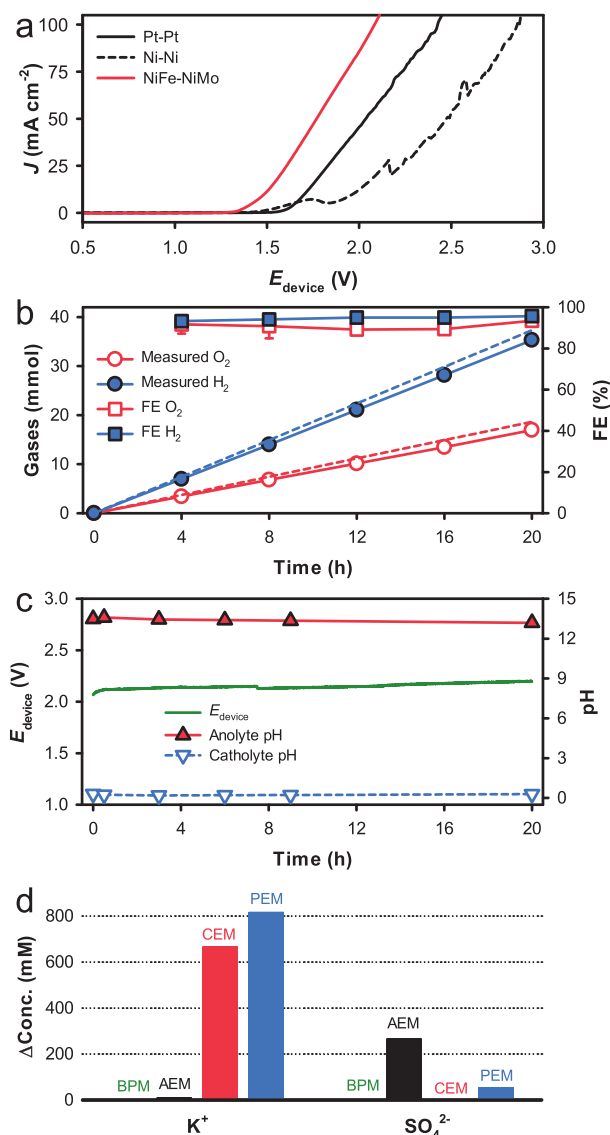

Fig. 6. (a–c) Electrochemical behaviors of NiFe-LDH anode and NiMo cathode pairs in two-cell devices divided by a BPM with anolyte of 1 M KOH and catholyte of 1 M H$_2$SO$_4$. (a) J-E_{device} curves. A Pt anode-Pt cathode pair and a Ni anode-Ni cathode pair were also compared. (b) Time-profiled O$_2$ and H$_2$ production from the anolyte and catholyte, respectively, and their FE values at $J = 100$ mA cm^{-2}. The dashed lines represent 100 % FEs of O$_2$ and H$_2$ production. (c) Changes in E_{device} and electrolyte pH values with time at $J = 100$ mA cm^{-2}. (d) Amounts of K$^+$ and SO$_4^{2-}$ transferred through a BPM between anolyte and catholyte after 4 h at $J = 100$ mA cm^{-2}. Other membranes (AEM, CEM, and PEM) were also compared under the same electrolysis conditions.

3.3. Desalination-coupled electrocatalysis

Electrocatalysis with the NiFe-LDH anode and NiMo cathode pair was coupled with the desalination of saline water by designing a desalination cell (0.171 M NaCl) between the anolyte (1 M KOH) and catholyte (1 M H$_2$SO$_4$) (Scheme 1b). To further use the desalted ions, each acid cell (0.1 M NaCl, pH ~6) and base cell (0.1 M NaCl, pH ~6) was placed between the desalination cell and electrode cells. At $J = 10$ mA cm^{-2}, E_{device} of ~2.4 V in the initial stage gradually increased over 10 h, while the ionic conductivity (σ) of saline water in the desalination cell decreased linearly with time (Fig. 7a). The decrease in σ was attributed to the transfer of Cl$^-$ and Na$^+$ from the saline water to the acid and base cells, respectively, which increased the overall resistivity of the device. The gradual increases in the concentrations of Cl$^-$ and Na$^+$ in the acid
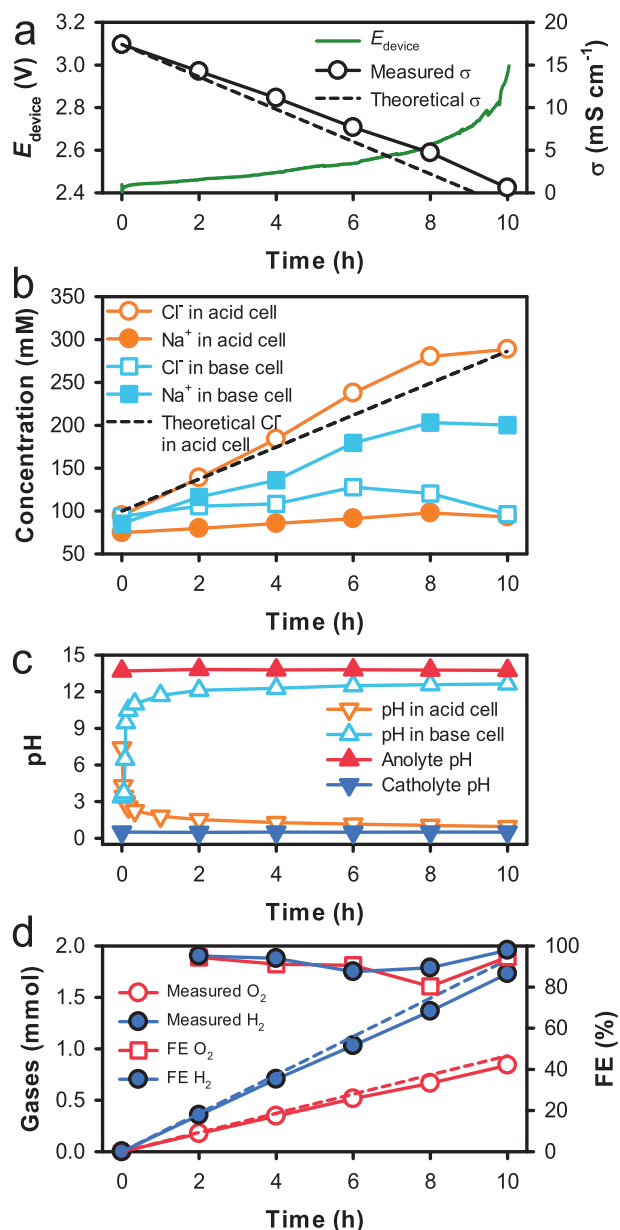
Fig. 7. Desalination-coupled electrocatalytic unit device with NiFe-LDH anode and NiMo cathode at $J = 10$ mA cm^{-2} (Case Study I in Table 1). For the device construction, see Scheme 1b. (a) Changes in E_{device} and ionic conductivity (σ) of saline water with electrolysis time. The dashed line represents the theoretical σ based on J. (b) Changes in concentrations of desalted ions (Cl$^-$ and Na$^+$). The dashed line represents the theoretical Cl$^-$ concentration in the acid cell. (c) Changes in pH values in the solutions in the acid and base cells, and electrolytes. (d) Time-profiled O$_2$ and H$_2$ production from the anolyte and catholyte, respectively, and their FE values. The dashed lines represent 100 % FEs of O$_2$ and H$_2$ production.

and base cells, respectively, confirmed the counter flow of each ion (Fig. 7b). Simultaneously, the pH values in the acid and base cells changed to ~1 and ~12.5, respectively, owing to the continuous supply of H$^+$ and OH$^-$ from the BPM next to the acid cell (BPM-a) and the other next to the base cell (BPM-b), respectively (Fig. 7c). This indicates that the acid and base cells were enriched with HCl and NaOH, respectively. However, the anolyte and catholyte pH values remained unchanged owing to the supply of OH$^-$ and H$^+$ from BPM-a and BPM-b, respectively. The observed concentration changes in the desalted ions were quite similar to the theoretical values estimated based on J. Slight

deviations were attributed to the imperfect functions of the employed commercial ion-exchange membranes. Assuming ideal ion transport, the pH values in the acid and base cells should be changed to ~0.77 and ~13.2, respectively, upon complete desalination of saline water. Nevertheless, the overall ITE was 85 % (Case Study I in Table 1). O$_2$ and H$_2$ were linearly produced at 0.173 and 0.084 mmol cm^{-2} h^{-1} with desalination-electrolysis time in the anolyte and catholyte, respectively, with FE values of >90 % (Fig. 7d). The SEC was estimated to be 6.58 kWh m^{-3}, which is ~35 % lower than that in our previous report [12]. This low SEC is impressive considering the concurrent production of many value-added chemicals (H$_2$, HCl, and NaOH) in the employed system.

An increase in the initial NaCl concentrations (0.1 M to 0.2 M) in the acid and base cells insignificantly influenced the desalination behavior (Case Study II; Fig. S8). For example, the 50 % desalination time ($\tau_{1/2}$) was 5.6 h and the ITE was 82 %. The SEC increased marginally to ~7 kWh m^{-3}. When HCl (0.1 M) and NaOH (0.1 M) were used instead of NaCl (0.1 M) in the acid and base cells, respectively, the overall device performance remained unchanged, with a similar ITE of ~85 % and SEC of 6.62 kWh m^{-3} (Case Study III; Fig. S9). The initial pH values of 1.75 and 12.94 with the acid and base cells gradually changed during electrolysis and reached 0.70 and 13.21, respectively, upon 100 % desalination, yielding HCl of ~160 mM and NaOH of ~152 mM. However, when J was 10-fold higher (100 mA cm^{-2}), the desalination process kinetics was enhanced 10-fold and completed in 1 h ($\tau_{1/2}$ ~0.6 h) (Case Study IV; Fig. S10). This suggests that the overall desalination kinetics depended solely on J. However, SEC increased by 2.4 times (15.8 kWh m^{-3}) even though the total amount of charges ($J \times \tau_{1/2}$) was similar to that in the Case Study III.

To reduce SEC while enhancing desalination kinetics, five desalination cells were arrayed between the acid and base cells by alternately placing AEM and CEM (Scheme 1c). As shown in Fig. 8, several different behaviors were observed from those with the desalination cell unit device (Scheme 1b). First, the initial E_{device} value (~3.0 V) at $J = 10$ mA cm^{-2} was slightly increased, because the device resistance was increased by membranes with a maximum of ~40 Ω/sq. per membrane. Second, the desalination kinetics was significantly enhanced even with the increase in the saline water volume by two times (Case Study V). Desalination was completed in 4 h, with $\tau_{1/2}$ of ~2 h. Such the enhanced kinetics was attributed to an enlarged ion-exchange membrane area in contact with saline water, leading to a large ITE of 417 %. However, the normalized ITE based on the number of desalination cells (417 %/5 cells = 83.4 %/cell) was similar to that obtained using the unit device (85 %). The as-observed ITE values of <100 % were attributed to sluggish ion transfer across the employed membranes, particularly at high J values (e.g., Case Study IV). Most notably, a significantly low SEC value (1.79 kWh m^{-3}) was obtained, corresponding to 27 % of that obtained with the unit device (Case Study I) and comparable to those of the state-of-the-art processes in the literature [25,26].

Finally, the multi-desalination cell array device was tested for desalination of seawater (36 g L^{-1}) (Case Study VI; Fig. S11). The initial E_{device} value was similar to that of the brackish water (0.171 M NaCl). However, a 3-fold long $\tau_{1/2}$ (6.4 h) was required because of the nearly 3-fold higher salinity of seawater compared to that of brackish water. Considering only the Na$^+$ and Cl$^-$ transfers, the ITE was estimated to be ~360 %. When other ions present in seawater (e.g., SO$_4^{2-}$, Mg^{2+}, Ca^{2+}, and K$^+$) were included, the ITE increased to ~400 %. The pH values of the acidic and basic cells changed to <1 and >12, respectively. All these results demonstrate that the overall device performance with seawater was similar to that with brackish water, despite a more complicated matrix of the former. Despite the prevention of seawater ion contact to both the anode and cathode, scaling and fouling issues with the membranes still linger. However, they can be partly addressed with the electrodialysis reversal process which is effective in removing the adsorbed ions on the membrane surface [43].
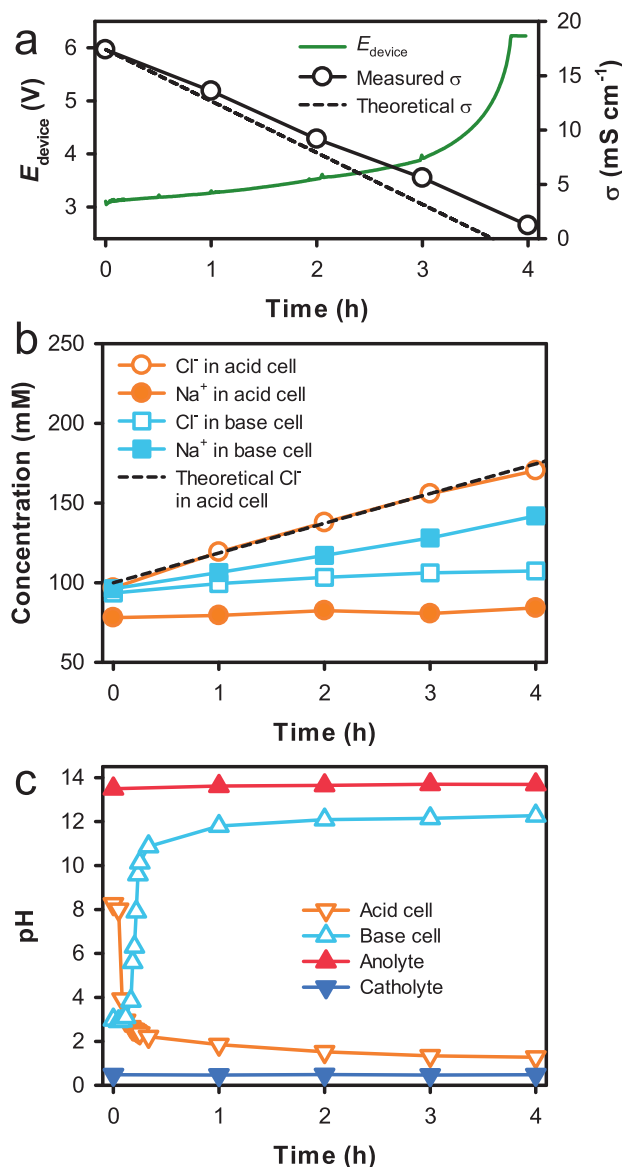
Fig. 8. Desalination-coupled electrocatalytic stack device with NiFe-LDH anode and NiMo cathode at $J = 10$ mA cm^{-2} (Case Study V in Table 1). For the device construction, see Scheme 1c. (a) Changes in E_{device} and ionic conductivity (σ) of saline water with electrolysis time. The dashed line represents the theoretical σ based on J. (b) Changes in concentrations of desalted ions (Cl$^-$ and Na$^+$). The dashed line represents the theoretical Cl$^-$ concentration in the acid cell. (c) Changes in pH values in the solutions in the acid and base cells, and electrolytes.

4. Conclusions

In this study, desalination-coupled electrolyzers with NiFe-LDH anode and NiMo cathode pairs were designed. The devices, equipped with BPMs, AEMs, and CEMs, successfully desalinated brackish water and seawater via electrocatalytic OER and HER with the electrode pairs, while HCl and NaOH were simultaneously produced. The as-synthesized NiFe-LDH anode showed η$_{OER}$ as low as those with noble metal catalysts in a 1 M KOH solution. The binary NiMo cathode also exhibited a low η$_{HER}$ in 1 M H$_2$SO$_4$ solution. The electrode pair divided by BPM required only η$_{10}$ and η$_{100}$ of ~0.35 V and ~0.90 V, respectively, for overall water splitting with FEs of >95 % for OER and HER at $J = 100$ mA cm^{-2} over 20 h, while initial pH values of anolyte and catholyte were maintained. The electrode pair was further demonstrated to drive the desalination of

saline water, OER, HER, and concurrent production of HCl and NaOH in a single device. The SEC for 50 % desalination was ~6.6 kWh m^{-3} using the unit device. When the desalination cell was stacked, the SEC was reduced to ~1.8 kWh m^{-3} while the other processes (OER, HER, and production of HCl and NaOH) were not altered. The pH values of the anolyte and catholyte were unchanged due to the continual supply of OH$^-$ and H$^+$ via the OER and HER, respectively, keeping the electrode pair intact. The proposed multi-functional electrolyzer is highly promising for converting electrical energy into hydrogen energy, simultaneously desalinating saline water, and producing value-added chemicals.

CRediT authorship contribution statement

Byeong-ju Kim: Methodology, Validation, Formal analysis, Investigation. **Ho Kyong Shon:** Writing – review & editing. **Dong Suk Han:** Formal analysis, Writing – review & editing, Funding acquisition. **Hyunwoong Park:** Conceptualization, Methodology, Validation, Formal analysis, Resources, Writing – original draft, Writing – review & editing, Visualization, Supervision, Project administration, Funding acquisition.

Declaration of competing interest

The authors declare that they have no known competing financial interests or personal relationships that could have appeared to influence the work reported in this paper.

Data availability

Data will be made available on request.

Appendix A. Supplementary data

Supplementary data to this article can be found online at https://doi.org/10.1016/j.desal.2023.116431.

References

[1] The Future of Hydrogen: Seizing Today's Opportunities, International Energy Agency, 2019. June.
[2] N.S. Lewis, Powering the planet, MRS Bull. 32 (2007) 808–820, https://doi.org/10.1557/mrs2007.168.
[3] K. Zeng, D. Zhang, Recent progress in alkaline water electrolysis for hydrogen production and applications, Prog. Energy Combust. Sci. 36 (2010) 307–326, https://doi.org/10.1016/j.pecs.2009.11.002.
[4] J. Ivy, Summary of Electrolytic Hydrogen Production: Milestone Completion Report, National Renewable Energy Laboratory, 2004 (NREL/MP-560-36734), September.
[5] A. Christensen, Assessment of Hydrogen Production Costs From Electrolysis: United States And Europe, The International Council on Clean Transportation, June 4, 2020.
[6] H. Park, Solar remediation of wastewater and saline water with concurrent production of value-added chemicals, J. Environ. Chem. Eng. 10 (2022), 106919, https://doi.org/10.1016/j.jece.2021.106919.
[7] S. Bolar, S. Shit, N. Chandra Murmu, T. Kuila, Progress in theoretical and experimental investigation on seawater electrolysis: opportunities and challenges, Sustain. Energy Fuels 5 (2021) 5915–5945, https://doi.org/10.1039/d1se01347e.

[8] S. Dresp, F. Dionigi, M. Klingenhof, P. Strasser, Direct electrolytic splitting of seawater: opportunities and challenges, ACS Energy Lett. 4 (2019) 933–942, https://doi.org/10.1021/acsenergylett.9b00220.

[9] N.N. Liang, D.S. Han, H. Park, Membraneless unbuffered seawater electrolysis for pure hydrogen production using PtRuTiOx anode and MnOx cathode pairs, Appl. Catal. BEnviron. 324 (2023) 12275, https://doi.org/10.1016/j.apcatb.2022.122275.

[10] T. Elmakki, S. Zavahir, M. Gulied, H. Qiblawey, B. Hammadi, M. Khraisheh, H. K. Shon, H. Park, D.S. Han, Potential application of hybrid reverse electrodialysis (RED)-forward osmosis (FO) system to fertilizer-producing industrial plant for efficient water reuse, Desalination 550 (2023), 116374, https://doi.org/10.1016/j.desal.2023.116374.

[11] F. Sun, J. Qin, Z. Wang, M. Yu, X. Wu, X. Sun, J. Qiu, Energy-saving hydrogen production by chlorine-free hybrid seawater splitting coupling hydrazine degradation, Nat. Commun. 12 (2021) 4182, https://doi.org/10.1038/s41467-021-24529-3.

[12] B.-J. Kim, G. Piao, S. Kim, S.Y. Yang, Y. Park, D.S. Han, H.K. Shon, M.R. Hoffmann, H. Park, High efficiency solar desalination accompanying electrocatalytic conversions of desalted chloride and captured carbon dioxide, ACS Sustain. Chem. Eng. 7 (2019) 15320–15328, https://doi.org/10.1021/acssuschemeng.9b02640.

[13] Y.Y. Ahn, S.Y. Yang, C. Choi, W. Choi, S. Kim, H. Park, Electrocatalytic activities of Sb-SnO2 and Bi-TiO2 anodes for water treatment: effects of electrocatalyst composition and electrolyte, Catal. Today 282 (2017) 57–64, https://doi.org/10.1016/j.cattod.2016.03.011.

[14] K.S. Exner, J. Anton, T. Jacob, H. Over, Controlling selectivity in the chlorine evolution reaction over RuO2-based catalysts, Angew. Chem. Int. Ed. 126 (2014) 11212–11215, https://doi.org/10.1002/ange.201406112.

[15] C. Deslouis, D. Festy, O. Gil, G. Rius, S. Touzain, B. Tribollet, Characterization of calcareous deposits in artificial sea water by impedance techniques - I. Deposit of CaCO3 without Mg(OH) (2), Electrochim. Acta 43 (1998) 1891–1901, https://doi.org/10.1016/S0013-4686(97)00303-4.

[16] H. Karoui, B. Riffault, M. Jeannin, A. Kahoul, O. Gil, M. Ben Amor, M.M. Tlili, Electrochemical scaling of stainless steel in artificial seawater: role of experimental conditions on CaCO3 and Mg(OH) (2) formation, Desalination 311 (2013) 234–240, https://doi.org/10.1016/j.desal.2012.07.011.

[17] M.A. Khan, T. Al-Attas, S. Roy, M.M. Rahman, N. Ghaffour, V. Thangadurai, S. Larter, J. Hu, P.M. Ajayan, M.G. Kibria, Seawater electrolysis for hydrogen production: a solution looking for a problem? Energy Environ. Sci. 14 (2021) 4831–4839, https://doi.org/10.1039/D1EE00870F.

[18] J.N. Hausmann, R. Schlögl, P.W. Menezes, M. Driess, Is direct seawater splitting economically meaningful? Energy Environ. Sci. 14 (2021) 3679–3685, https://doi.org/10.1039/d0ee03659e.

[19] S.S. Veroneau, D.G. Nocera, Continuous electrochemical water splitting from natural water sources via forward osmosis, Proc. Natl. Acad. Sci. U. S. A. 118 (2021), e2024855118, https://doi.org/10.1073/pnas.2024855118.

[20] S. Kim, G. Piao, D.S. Han, H.K. Shon, H. Park, Solar desalination coupled with water remediation and molecular hydrogen production: a novel solar water-energy nexus, Energy Environ. Sci. 11 (2018) 344–353, https://doi.org/10.1039/C7EE02640D.

[21] S. Kim, D.S. Han, H. Park, Reduced titania nanorods and Ni-Mo-S catalysts for photoelectrocatalytic water treatment and hydrogen production coupled with desalination, Appl. Catal. BEnviron. 284 (2021), 119745, https://doi.org/10.1016/j.apcatb.2020.119745.

[22] S.Z. Oener, M.J. Foster, S.W. Boettcher, Accelerating water dissociation in bipolar membranes and for electrocatalysis, Science 369 (2020) 1099–1103, https://doi.org/10.1126/science.aaz1487.

[23] D. Vermaas, M. Sassenburg, W.A. Smith, Photo-assisted water splitting with bipolar membrane induced pH gradients for practical solar fuel devices, J. Mater. Chem. A 3 (2015) 19556–19562, https://doi.org/10.1039/C5TA06315A.

[24] M.D. Eisaman, K. Parajuly, A. Tuganov, C. Eldershaw, N. Chang, K.A. Littau, CO2 extraction from seawater using bipolar membrane electrodialysis, Energy Environ. Sci. 5 (2012) 7346–7352, https://doi.org/10.1039/c2ee03393c.

[25] S. Gorjian, B. Ghobadia, H. Ebadi, F. Ketabchi, S. Khanmohammadi, Applications of solar PV systems in desalination technologies, in: S. Gorijan, A. Shukla (Eds.), Photovoltaic Solar Energy Conversion: Technologies, Applications And Environmental Impacts, Elsevier, 2020.

[26] S.K. Patel, M. Qin, W.S. Walker, M. Elimelech, Energy efficiency of electro-driven brackish water desalination: electrodialysis significantly outperforms membrane capacitive deionization, Environ. Sci. Technol. 54 (2020) 3663–3677, https://doi.org/10.1021/acs.est.9b07482.

[27] F. Song, L. Bai, A. Moysiadou, S. Lee, C. Hu, L. Liardet, X. Hu, Transition metal oxides as electrocatalysts for the oxygen evolution reaction in alkaline solutions: an application-inspired renaissance, J. Am. Chem. Soc. 140 (2018) 7748–7759, https://doi.org/10.1021/jacs.8b04546.

[28] M.S. Burke, L.J. Enman, A.S. Batchellor, S. Zou, S.W. Boettcher, Oxygen evolution reaction electrocatalysis on transition metal oxides and (oxy)hydroxides: activity trends and design principles, Chem. Mater. 27 (2015) 7549–7558, https://doi.org/10.1021/acs.chemmater.5b03148.

[29] Z. Cai, X. Bu, P. Wang, J.C. Ho, J. Yang, X. Wang, Recent advances in layered double hydroxide electrocatalysts for the oxygen evolution reaction, J. Mater. Chem. A 7 (2019) 5069–5089, https://doi.org/10.1039/C8TA11273H.

[30] Q. Xiang, F. Li, W. Chen, Y. Ma, Y. Wu, X. Gu, Y. Qin, P. Tao, C. Song, W. Shang, H. Zhu, T. Deng, J. Wu, In situ vertical growth of Fe–Ni layered double-hydroxide arrays on Fe–Ni alloy foil: interfacial layer enhanced electrocatalyst with small overpotential for oxygen evolution reaction, ACS Energy Lett. 3 (2018) 2357–2365, https://doi.org/10.1021/acsenergylett.8b01466.

[31] T. Wang, X. Wang, Y. Liu, J. Zheng, X. Li, A highly efficient and stable biphasic nanocrystalline Ni–Mo–N catalyst for hydrogen evolution in both acidic and alkaline electrolytes, Nano Energy 22 (2016) 111–119, https://doi.org/10.1016/j.nanoen.2016.02.023.

[32] C.C.L. McCrory, S. Jung, I.M. Ferrer, S.M. Chatman, J.C. Peters, T.F. Jaramillo, Benchmarking hydrogen evolution reaction and oxygen evolution reaction electrocatalyts for solar watre splitting devices, J. Am. Chem. Soc. 137 (2015) 4347–4357, https://doi.org/10.1021/ja510442p.

[33] A. Nairan, P. Zou, C. Liang, J. Liu, D. Wu, P. Liu, C. Yang, NiMo solid solution nanowire array electrodes for highly efficient hydrogen evolution reaction, Adv. Funct. Mater. 29 (2019), 1903747, https://doi.org/10.1002/adfm.201903747.

[34] E. Navarro-Flores, Z.W. Chong, S. Omanovic, Characterization of Ni,NiMo, NiW and NiFe electroactive coatings as electrocatalysts for hydrogen evolution in an acidic medium, J. Mol. Catal. A Chem. 226 (2005) 179–197, https://doi.org/10.1016/j.molcata.2004.10.029.

[35] D.E. Sachit, J.N. Veenstra, Analysis of reverse osmosis membrane performance during desalination of simulated brackish surface waters, J. Membr. Sci. 453 (2014) 136–154, https://doi.org/10.1016/j.memsci.2013.10.051.

[36] A.P. Grosvenor, M.C. Biesinger, R.S. Smart, N.S. McIntyre, New interpretations of XPS spectra of nickel metal and oxides, Surf. Sci. 600 (2006) 1771–1779, https://doi.org/10.1016/j.susc.2006.01.041.

[37] J. Liu, J.S. Wang, B. Zhang, Y.J. Ruan, L. Lv, X. Ji, K. Xu, L. Miao, J.J. Jiang, Hierarchical NiCo2S4@NiFe LDH heterostructures supported on nickel foam for enhanced overall-water-splitting activity, ACS Appl. Mater. Interfaces 9 (2017) 15364–15372, https://doi.org/10.1021/acsami.7b00019.

[38] Y.K. Kim, J.H. Kim, Y.H. Jo, J.S. Lee, Precipitating metal nitrate deposition of amorphous metal oxyhydroxide electrodes containing Ni,Fe, and Co for electrocatalytic water oxidation, ACS Catal. 9 (2019) 9650–9662, https://doi.org/10.1021/acscatal.9b02701.

[39] T.H. Jeon, W. Choi, H. Park, Cobalt-phosphate complexes catalyze the photoelectrochemical water oxidation of BiVO4 electrodes, Phys. Chem. Chem. Phys. 13 (2011) 21392–21401, https://doi.org/10.1039/c1cp23135a.

[40] S.K. Choi, W. Choi, H. Park, Solar water oxidation using nickel-borate coupled BiVO4 photoelectrodes, Phys. Chem. Chem. Phys. 15 (2013) 6499–6507, https://doi.org/10.1039/c3cp00073g.

[41] B.G. Kim, J. Park, W. Choi, D.S. Han, J. Kim, H. Park, Electrocatalytic arsenite oxidation using iron oxyhydroxide polymorphs (α-, β-, and γ-FeOOH) in aqueous bicarbonate solution, Appl. Catal. BEnviron. 283 (2021), 119608, https://doi.org/10.1016/j.apcatb.2020.119608.

[42] L. Negahdar, F. Zeng, S. Palkovits, C. Broicher, R. Palkovits, Mechanistic aspects of the electrocatalytic oxygen evolution reaction over Ni-Co oxides, ChemElectroChem 6 (2019) 5588–5595, https://doi.org/10.1002/celc.201901265.

[43] D.A. Vermaas, D. Kunteng, J. Veerman, M. Saakes, K. Nijmeijer, Periodic feedwater reversal and air sparging as antifouling strategies in reverse electrodialysis, Environ. Sci. Technol. 48 (2014) 3065–3073, https://doi.org/10.1021/es4045456.